RSC Advances

PAPER

View Article Online
View Journal | View Issue

Cite this: *RSC Adv.*, 2020, **10**, 16892

Enhanced photocatalytic activity of a visible-light-driven ternary $WO_3/Ag/Ag_3PO_4$ heterojunction: a discussion on electron transfer mechanisms†

Shengqi Zhang,[a] Tao Yu,[a] Hui Wen,[a] Rui Guo, *[abc] Juanjuan Xu,*[ac] Ruixia Zhong,*[ac] Xian Li[ac] and Junhua You[d]

Received 23rd February 2020
Accepted 22nd April 2020

DOI: 10.1039/d0ra01731k

rsc.li/rsc-advances

WO_3/Ag_3PO_4 with different weight ratios were prepared by ultrasonic assisted two-step deposition method. The as-prepared samples were characterized by X-ray diffraction (XRD), scanning electron microscopy (SEM), photoluminescence spectroscopy (PL) and transmission electron microscopy (TEM). The photocatalytic activities of all samples were evaluated by the degradation of rhodamine B (RhB) under visible light irradiation. WA-60 shows the highest photocatalytic activity in the WA-*x* series composite, while the photocatalytic activity of WAA-60 is the best among all samples. The free radical trapping experiments show that photogenerated holes (h^+) are the main active species. The Ag nanoparticles produced by the decomposition of Ag_3PO_4 are located at the interface of Ag_3PO_4/WO_3, which promotes the separation efficiency of photogenerated electrons and holes. To further explain the photocatalytic mechanism, electrochemical and physical tests are introduced to explore the flow of electrons inside the catalyst.

1. Introduction

In recent decades, semiconductor photocatalysis has attracted widespread attention due to its increasing utilization in the removal of organic contaminants. TiO_2, as the representative of the most commonly used semiconductor photocatalysts, can only be excited by ultraviolet light because of its wide bandgap of 3.2 eV, the shortcoming being the utilization of only 4% of solar energy at most.[1,2] Therefore, the further study of visible-light-responsive photocatalysts has become one of the hot topics.[3,4]

Metal oxide semiconductors are considered promising photocatalysts due to their strong absorption of visible light and catalytic ability to convert light energy into chemical energy. Amongst them, WO_3 has attracted great concern owning to the suitable bandgap (2.4–2.8 eV), outstanding physicochemical properties and stability. However, the photocatalytic activity of pure WO_3 is limited by its large electron–hole recombination rate.[5] Ag_3PO_4 is also a visible-light-driven photocatalyst with a high photodegradation rate of organic dyes.[6] However, Ag_3PO_4 is so photosensitive that it is slightly soluble in aqueous solution and some Ag^+ can be reduced to Ag nanoparticles, located on the surface. Therefore, photocatalytic activity is gradually deteriorating, which is the major obstacle of Ag_3PO_4 as a stable photocatalyst.[7]

A variety of methods have been used to improve the photocatalytic activity of semiconductors. One of these methods is to build heterogeneous semiconductor composites. Semiconductor heterojunctions can extend the spectral range of light absorption and inhibit the recombination of photoinduced electron and hole due to classic type II heterojunction or Z-scheme mechanism.[8,9] WO_3 is, therefore, coupled with other semiconductors, such as $AgIO_3$,[10] g-C_3N_4,[11–13] CdS,[14] C-dots,[15] to form different heterojunction, *etc.* Among these semiconductors, Ag_3PO_4 is considered as one of the most promising materials due to its suitable band structure in relation to that of WO_3.[16] which has been studied in several important literatures.[17–24] For instance, Lu *et al.*[17] reported that the enhanced properties of the WO_3/Ag_3PO_4 composites could be attributed to the synergistic effect of higher surface area, matched band structure, strong light absorption, and high electron–hole separation rate. Xu[18,19] *et al.* reported a series of three-dimensional ordered macroporous WO_3 (3DOM WO_3) composited Ag_3PO_4 photocatalysts, and explored the reasons improving photocatalytic performance. In addition, Bu *et al.*[20] reported a Z-scheme photocatalyst by introducing Ag in Ag_3PO_4/WO_3-X, which was achieved by using the weak reducibility of

[a]*School of Materials Science and Engineering, Northeastern University, Shenyang 110819, China. E-mail: guorui@neuq.edu.cn; 1519931572@qq.com; 46028914@qq.com*

[b]*Key Laboratory of Advanced Energy Materials Chemistry (Ministry of Education), College of Chemistry, Nankai University, Tianjin 300071, China*

[c]*School of Resources and Materials, Northeastern University at Qinhuangdao, 066004, China*

[d]*School of Materials Science and Engineering, Shenyang University of Technology, Shenyang 110870, China*

† Electronic supplementary information (ESI) available. See DOI: 10.1039/d0ra01731k

$WO_{2.72}$ and depositing Ag nanoparticles onto the surface of $WO_{2.72}$. The work of Cai *et al.*[21] further focused on carriers transfer in Ag_3PO_4-WO_3/multi-walled carbon nanotubes to explain the photocatalytic mechanism.

Inspired by the above studies, WO_3/Ag/Ag_3PO_4 ternary heterojunctions were prepared.[25] Subsequently, the effects of Ag nanoparticles on the performances of the composite photocatalysts are discussed by analyzing the electron structures and the flows of photogenerated carriers.

2. Materials and methods

2.1 Preparation

Preparation of WO_3. First, 1 mmol of $H_{40}N_{10}O_{41}W_{12}\cdot xH_2O$ and 50 mg of CTAB was added to 500 mL of deionized water, and the mixture was ultrasonically dispersed for about 60 minutes until the mixture was completely homogeneous. Then, the nitric acid was gradually added to the previous solution until the solution completely turned yellow, subsequently, keeping magnetic stirring for 24 hours. The obtained mixed solution was suction filtered, washed with deionized water and ethanol, and then dried at 80 °C overnight. Finally, WO_3 powder was obtained by calcining at 500 °C for 12 h.

Preparation of WO_3/Ag_3PO_4. WO_3/Ag_3PO_4 (WA) photocatalysts with different weight ratios were prepared by a simple ultrasound-assisted deposition route at room temperature. Typically, $AgNO_3$ and as-prepared WO_3 powder with different ratio were added to 500 mL of deionized water, then the mixture was ultrasonically treated for 30 min. Subsequently, the Na_2HPO_4 solution was added dropwise to the above solution under stirring for 2 hours. The collected catalyst was vacuum dried at 80 °C overnight, labeled as WA-*x*, where *x* represents the Ag_3PO_4 weight percentage.

Preparation of WO_3/Ag/Ag_3PO_4. The above WA-60 sample was exposed to light for different time. Then, after centrifuged and washed with deionized water and ethanol, WO_3/Ag/Ag_3PO_4 composite was obtained by dried at 80 °C for 12 h, labeled as WAA-*x*, *x* representing the time of irradiation.

2.2 Characterization

The crystalline structures of the samples were identified by powder X-ray diffraction (XRD) using a D/Max-RB X-ray diffractometer equipped with Cu Kα radiation at the scan rate (2θ) of 0.08° s^{-1} from 10 to 90°. The morphologies and microstructures characterizations were performed on the SEM (Zeiss Supra 55) and HRTEM (FEI Tecnai F30) measurements. The specific surface areas were determined by the nitrogen gas adsorption method (V-Sorb 2800P). XPS spectrum was recorded on a PHI 5000C ESCA X-ray photo-electron spectrometer with a Mg K excitation source was used to surface analysis at 14.0 kV and 25 mA. The UV-Vis diffuse reflectance spectra (DRS) were determined on a scan UV-Vis spectrometer (RF 5301) with $BaSO_4$ as the reference sample. FT-IR experiment was carried out on FT-IR spectrometer (FTIR, 8400S, Shimadzu) in a KBr pellet, scanning from 400 to 4000 cm^{-1} at room temperature. Raman spectra were analyzed using the Raman spectrometer (HR-800), scanning from 100 to 1300 cm^{-1}. Photoluminescence spectra (PL) were measured by using a fluorescence spectrophotometer (Shimadzu RF-5301 PC) equipped with a Xenon lamp at an excitation wavelength of 280 nm. Electrochemical impedance spectroscopy (EIS) and Mott–Schottky (MS) tests of electrochemical measurements were performed on a electrochemical workstation with a three-electrode system (PARSTAT 2273) including a fluorine-doped tin oxide (FTO) glass electrode (working electrode), a platinum electrode (counter electrode), and a saturated calomel electrode (SCE, reference electrode). The work function (Φ) of samples were tested on KP Technology (KP020).

2.3 Photocatalytic activities experiments

The photocatalytic performance of as-prepared samples was assessed by the degradation of 100 mL RhB (20 mg L^{-1}) aqueous solution under a visible light irradiation ($\lambda \geq 420$ nm) with a 300 W Xe lamp. 100 mg of powdered sample was dispersed in the RhB solution under stirring for 30 min to obtain desorption–adsorption equilibrium in dark. 3 mL of suspension was periodically taken out from the reactor every 30 min and the dispersed powder was removed by centrifugation. The clean transparent solution was analyzed by UV-Vis spectroscopy. The change of normalized concentration (C/C_0) in the photodegradation process of RhB solution is obtained by the dye absorption profile (554 nm).

3. Results and discussions

3.1 Characterizations

The crystal phase and phase purity of the as-prepared samples were analyzed by XRD patterns. In Fig. 1a, the diffraction peaks at 23.109°, 23.579°, 24.349°, 26.585°, 28.604°, 28.914°, 33.252°, 33.550° and 34.151° are indexed to (002), (020), (200), (120), (−112), (112), (022), (−202) and (202) planes of monoclinic phase WO_3 (PDF# 72-0677). The diffraction patterns of Ag_3PO_4 contain seven peaks at 29.7°, 33.3°, 36.5°, 52.7°, 55.1°, and 57.3°, corresponding to (200), (210), (211), (222), (320), and (321) (PDF# 84-0192), respectively.[4] After the deposition of Ag_3PO_4, the peaks of cubic Ag_3PO_4 can still be detected from the XRD patterns of WA-*x*, where the intensity of the WO_3 related diffraction peaks (23.109°, 23.579°, and 24.349°) decreases with the increase of the *x*.

In the FT-IR spectra of all samples (Fig. 1b), the strong and wide absorption peak around 3400 cm^{-1} can be attributed to the stretching vibration of O–H, while the two sharp regions at 1382 and 1655 cm^{-1} are assigned to the bending vibration of H–O–H of the water molecules.[26] In particular, for WO_3, the broad absorption peak at 600–900 cm^{-1} originates from the tensile vibration W–O–W linkage[27] and the peak at 965 cm^{-1} is ascribed to the tensile mode of the W=O bond.[28] For pure Ag_3PO_4 and WA-*x*, the characteristic peak at 550 cm^{-1} is attributed to O=P–O bending vibration, and the peaks around 862 and 1016 cm^{-1} are designated as P–O–P symmetric and asymmetric stretching vibration modes, respectively.[29] All characteristic peaks of Ag_3PO_4 and WO_3 can be observed in the

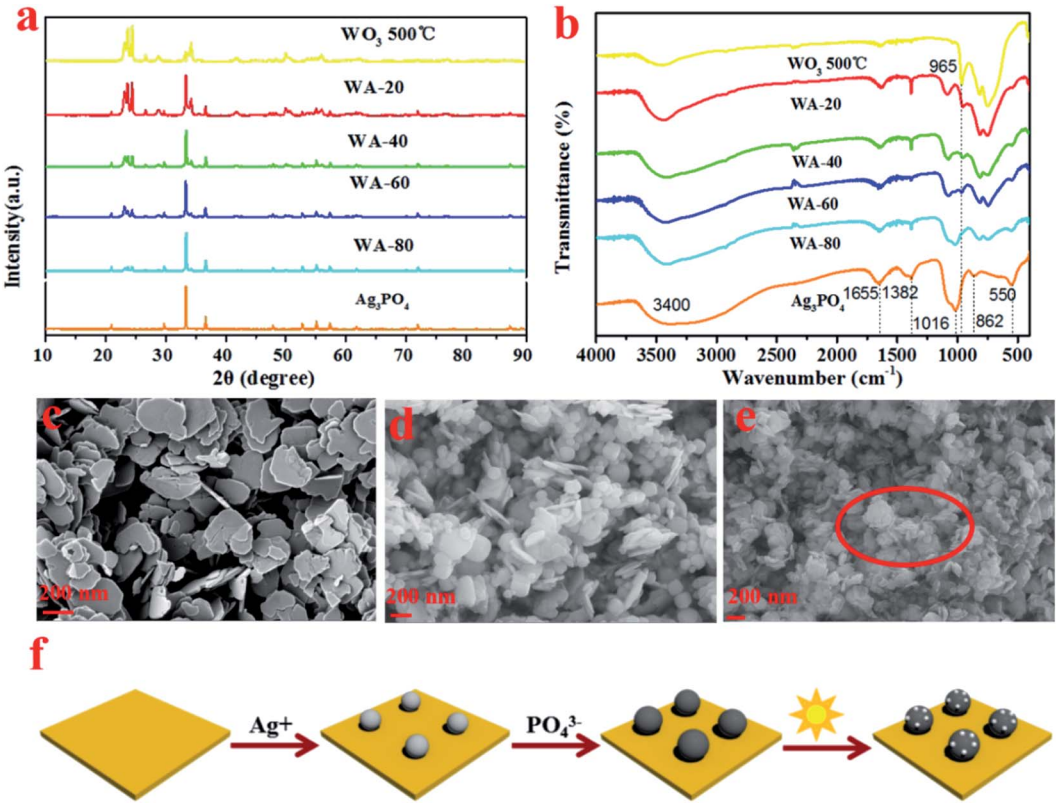

Fig. 1 XRD patterns of Ag_3PO_4, WO_3, and WA-*x*(a); FTIR spectra of Ag_3PO_4, WO_3, and WA-*x* (b); SEM images of WO_3, WA-60, and WAA-60 (c–e); schematic diagram of formation of WO_3/Ag/Ag_3PO_4 (f).

spectrum of the WA-*x* sample. Therefore, the above analyses endorse the coordination environment of W and P did not change significantly during the coupling process of WO_3 and Ag_3PO_4.

The SEM images of WO_3, WA-60, and WAA-60 are shown in Fig. 1. Fig. 1c exhibits the uniform WO_3 nanosheets with a thickness of 10–20 nm and a width of 100–160 nm, which facilitates the separate and transfer of electrons and holes.[30] It could be clearly observed that the Ag_3PO_4 were mainly deposited into the gaps between the adjacent WO_3 nanosheets, as shown in Fig. 1d. For the WAA-60 composites, as shown in Fig. 2e, it can be clearly observed that some small spots appeared on the surface of WAA-60 sample after the irradiation, which can be ascribed to the generation of Ag particles in the process of photoreduction. Moreover, the schematic diagram of the formation of WO_3/Ag_3PO_4 is shown in Fig. 1f.

Fig. 2 shows the high-resolution TEM image of WAA-60, the relatively crystallinity of the photocatalyst was perfect. More specifically, two different lattice fringes are clearly discerned (Fig. 2a) with a spacing of about 0.268 nm and 0.365 nm, which correspond to Ag_3PO_4 (210) and WO_3 (200), respectively.[31] As shown in Fig. 2b, some black dots can be observed clearly, whose composition is subsequently determined by the EDX-mapping. As shown in Fig. 2c–f, the distributions of Ag, P, and O elements in WAA-60 confirm the appearance of Ag nanoparticles (in the red circles).

Fig. 2g is XRD patterns of the WA-60 composite with different time of irradiation. Different irradiation time does not significantly affect the positions of the diffraction peaks, indicating that the crystal structures of Ag_3PO_4, WO_3, and WA-60 are retained. So the shape of peaks is still sharp. It is worth noting that the weak peak at 34.29° is the characteristic peak of Ag,[32] whose intensity increases with irradiation time, indicating that more Ag^+ is reduced.

High-resolution XPS is used to study the surface chemical state of the Ag_3PO_4, WA-60, and WAA-60. As shown in Fig. 3a, the XPS survey spectrum suggested that Ag, W, O, and P elements appear in WAA-*x*, being coincident with the constituent of the composites. In addition, detailed information of changes of valence state is studied from high-resolution XPS spectra in Fig. 3b–e. Fig. 3b shows the Ag 3d XPS spectra of Ag_3PO_4, WO_3, WA-60, and WAA-60. The peaks at 368 and 374 eV are attributed to Ag ($3d_{5/2}$) and Ag ($3d_{3/2}$), respectively, which could be fitted to two independent peaks corresponding to Ag^0 and Ag^+ ions.[33] For Ag_3PO_4, the peaks at 373.9 and 367.8 eV could be attributed to Ag^0.[19,24,34] For WA-60 and WAA-60, the peaks at 374.1 and 368 eV are attributed to Ag^0, and the peaks at 375.1 and 369 eV are assigned to Ag^+ ions.[35] The slight peak shifts are mainly due to the interaction between WO_3 and Ag_3PO_4. For the P 2p XPS spectra shown in Fig. 4c, all phosphorous are in the same oxidation state for Ag_3PO_4, WA-60, and WAA-60, having a broad peak at 132.8–133.0 eV for P^{5+} of PO_4^{3-}.[22] For the WO_3, the peaks of binding energy centered at

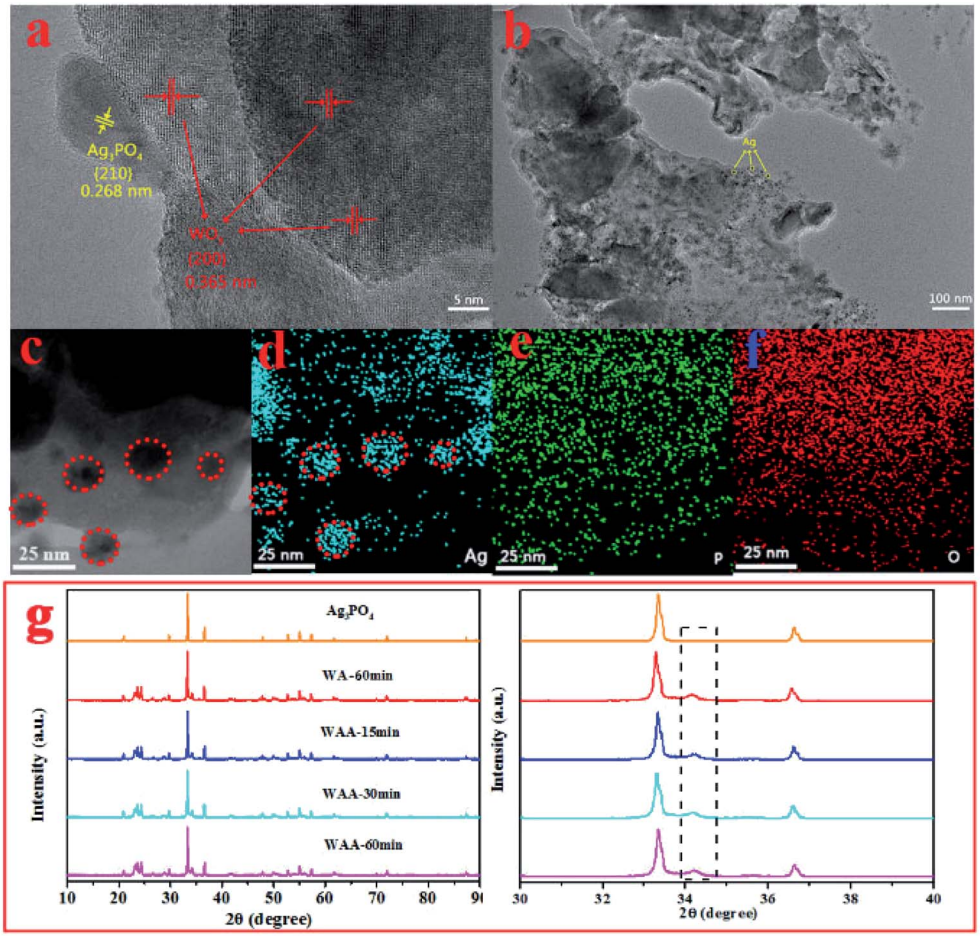

Fig. 2 HR-TEM images of WAA-60 (a); TEM images of WAA-60 (b), (c); element mapping of Ag (d), P (e) and O (f) in WAA-60; XRD patterns of Ag_3PO_4 and WAA-*x* (g).

37.193 and 35.055 eV can be assigned to W ($4f_{5/2}$) and W ($4f_{7/2}$), respectively, which can explain that W ion has a +6 charge.[26,36] Notably, the obvious blue shifts (*ca.* 0.7 eV) is displayed in the W 4f peaks of WA-60 and WAA-60 composites compared to pure WO_3, which could be related to the electron transferring from WO_3 to Ag particles.[37] The O 1s XPS spectra of WA-60 and WAA-60 is different after the combination of Ag_3PO_4 and WO_3 (Fig. 3e). For the Ag_3PO_4, the peak can be deconvoluted into two bands at 530.68 and 532.58 eV, which can be associated with the lattice oxygen atoms O^{2-} and oxygen of weakly adsorbed OH^- groups, respectively.[22] For the WO_3, the high-sensitivity XPS O 1s spectra are deconvolved into three peaks: the main peak at the lowest binding energy (529.88 eV) originated from the W–O bond in the WO_3 lattice;[38,39] the weak intensity band at about 531.68 eV corresponding to the existence of the hydroxyl group, *i.e.* the –OH bond, originated from water molecules; the highest energy band located at 533.08 eV corresponding to the C–O bonds.[40] In addition, it is observed that the O 1s spectrum in the WA-60 and WAA-60 composite samples are consistent with Ag_3PO_4, which may be related to the encapsulation of WO_3 by Ag_3PO_4.

Fig. 4a shows the FT-IR spectrum of Ag_3PO_4, WO_3, WA-60, and WAA-60. The absorption peaks of W=O bonds at 994 and 954 cm^{-1} in WAA-*x* are obviously observed due to the exposure of WO_3 after the photoetching of Ag_3PO_4 under irradiation.[41] Fig. 5b shows the Raman spectra of Ag_3PO_4, WO_3, WA-60, and WAA-60. For Ag_3PO_4, the peak centered at about 911 cm^{-1} is attributed to the PO_4^{3-} symmetric stretching vibration.[29] For WO_3, five typical peaks can be observed, including a peak at 134 cm^{-1} designated as lattice vibrations, 269 cm^{-1}, and 332 cm^{-1} due to δ (O–W–O) bending mode.[42] In addition, the peaks at 717 cm^{-1} and 809 cm^{-1} are derived from the ν (O–W–O) vibrational stretching mode of W–O–W bridging oxygen in WO_6 octahedral unit.[43–46]

3.2 Photocatalytic performance

Fig. 5a shows the degradation curves of RhB (20 mg L^{-1}) by Ag_3PO_4, WO_3, and WA-*x*. The WA-60 exhibits the highest photocatalytic activity. In addition, WA-20 has a poor effect for two reasons: one is that Ag_3PO_4 has a little specific gravity, and the other is that the interface between Ag_3PO_4 and WO_3 is not large enough and the surface area is reduced. However, for WAA-*x* series, above 94% of RhB are decomposed over WAA-60 photocatalyst after radiation for 120 min, as shown in Fig. 5b, while only 78% are removed within the same time using WA-60. It can

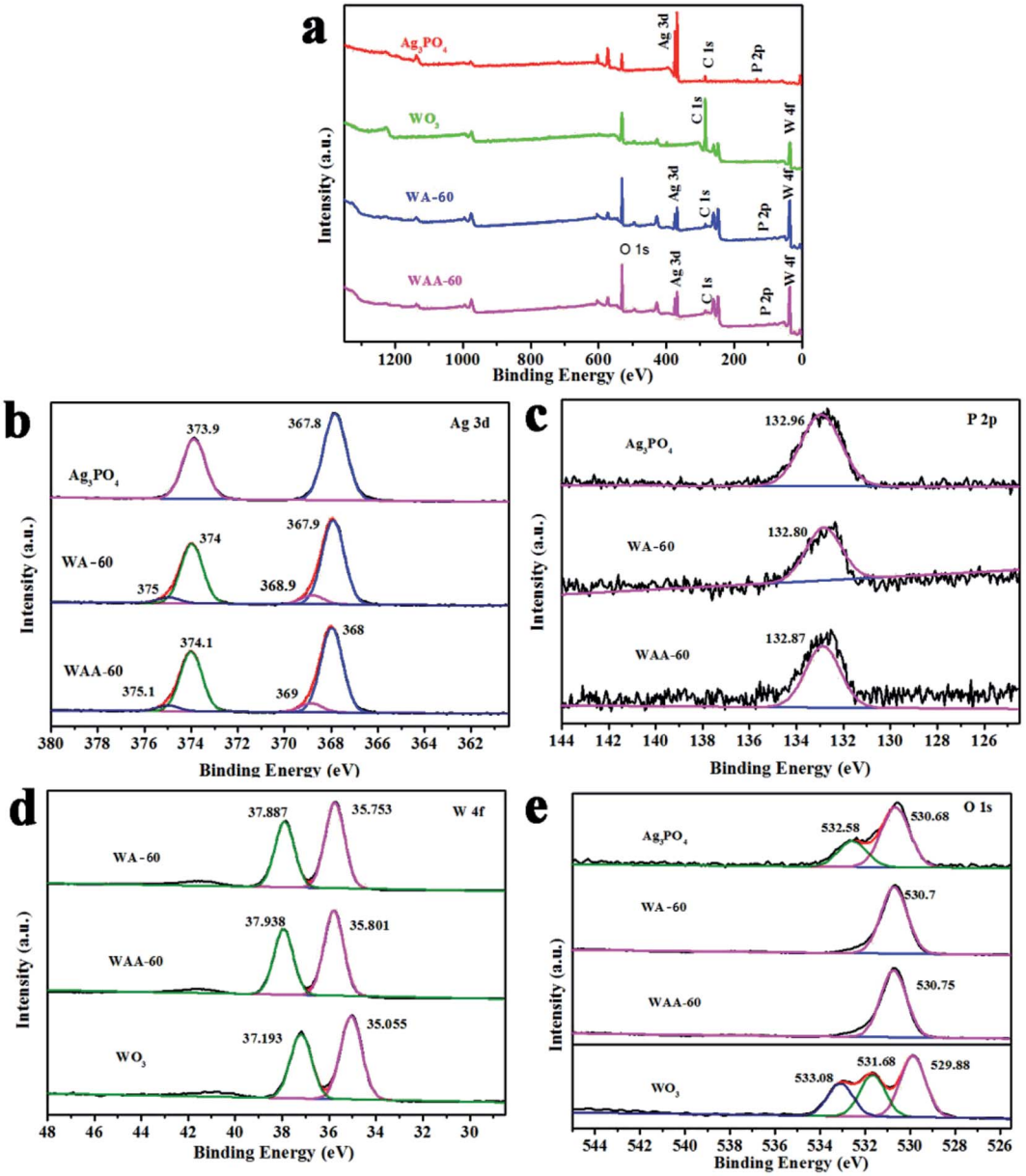

Fig. 3 XPS spectra of the total survey (a), Ag (b), P (c), W (d), and O (e) of Ag_3PO_4, WO_3, WA-60, and WAA-60.

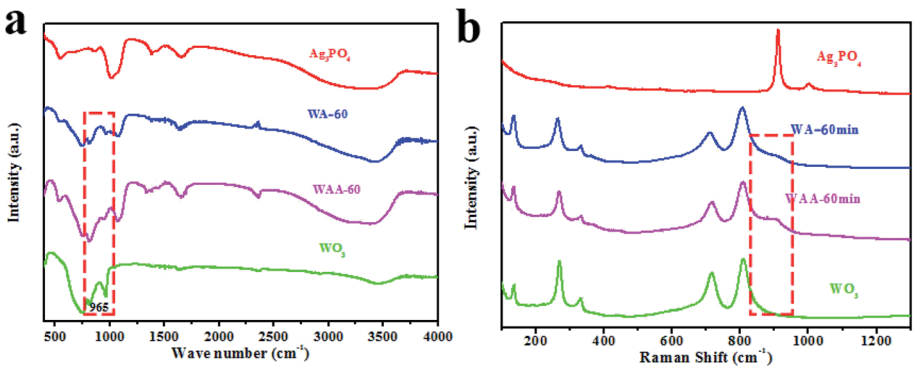

Fig. 4 FTIR spectra (a) and Raman spectra (b) of Ag_3PO_4, WA-60, WAA-60, and WO_3.

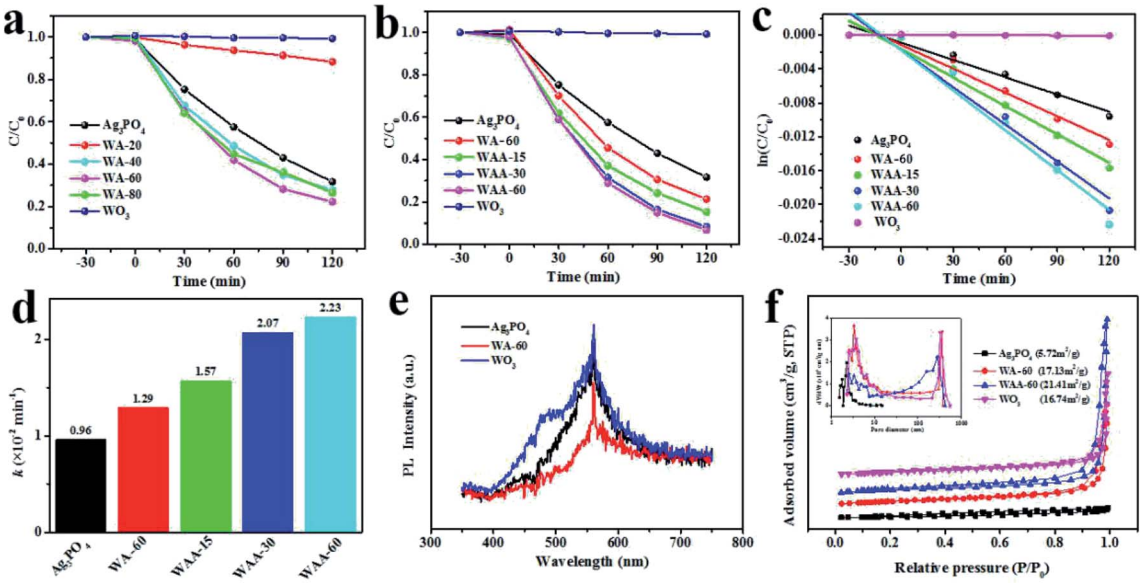

Fig. 5 The degradation of RhB of WA-*x* compared to WO_3 and Ag_3PO_4 (a), the degradation of RhB (b) and corresponding kinetics curves (c) over WAA-*x* compared to WO_3, Ag_3PO_4, and WA-60; comparison of the photocatalytic rate constant of bare Ag_3PO_4, WA-60, and WAA-*x* (d); PL emission spectra of Ag_3PO_4, WO_3, and WA-60 (e); and BET of Ag_3PO_4, WO_3, WA-60, and WAA-60 (f).

be found that the photodegradation process of RhB is a quasi-first-order reaction as shown in Fig. 5c. And the photocatalytic activities of the samples are also be evaluated by the apparent rate constant k[4] in Fig. 5d. The value of k of the WAA-60 reaches 2.23×10^{-2} min^{-1}, which is about 2.3 times lager than that of pure Ag_3PO_4 ($0.96\ 10^{-2}$ min^{-1}) and 1.7 times larger than WA-60 ($1.29\ 10^{-2}$ min^{-1}). The photocatalytic performance of the WAA-*x* sample is further improved by exposing to light, which can be attributed to the presence of Ag nanoparticles, giving rise to the enhanced separation efficiency of photogenerated electron–hole pairs. Besides, the degradation of MB is included in ESI, as shown in Fig. S1 and S2,† and the tendency of MB degradation is consistent with that of RhB.

In order to further investigate the photocatalytic performance of WO_3/Ag_3PO_4, PL and BET methods are introduced and summarized in Fig. 5e and f. As shown in Fig. 5e, a strong emission peaks of Ag_3PO_4, WO_3, and WA-60 appear at 569 nm. The intensity of the peak is related to the recombination efficiency of photogenerated electron–hole pairs.[47] WO_3 shows the greatest PL emission intensity, indicating its high recombination rate of photogenerated electron–hole pairs. In contrast, WA-60 shows a significantly lower PL emission intensity due to a better separation of photogenerated carriers between WO_3 and Ag_3PO_4. Fig. 5f is the N_2 adsorption–desorption isotherm and pore size distribution of Ag_3PO_4, WO_3, WA-60, and WAA-60. On the base of the IUPAC classification, Ag_3PO_4 exhibits a type III isotherm distribution, indicating a weak adsorbent–adsorbate interaction.[48] In addition, WA-60 and WAA-60 have isotherms of type IV with H3 hysteresis loops and their hysteresis deformation confirms the slit-like holes between the nanosheets. The BET surface areas of Ag_3PO_4, WO_3, WA-60, and WAA-60 are 5.72, 16.74, 17.13, and 21.41 m^2 g^{-1}, respectively. After normalized by surface area, the WAA-60 still has the best catalytic activity. The enhancement of the BET specific surface area of WAA-60 can be attributed to the photoetching of Ag_3PO_4. Moreover, it can be demonstrated that the increased surface area of the WAA-60 could play a positive role in enhancing the photocatalytic efficiency. In addition, WAA-60 samples have pores in two size ranges, which can be considered that the smaller mesopores are derived from the cracks within the WO_3 nanosheets, while the larger mesopores are produced by slits between WO_3 nanosheets,[21] which is consistent with the morphology of bare WO_3 in Fig. 1a.

In order to further study the main active substances directly involved in the photodegradation process of WO_3/Ag_3PO_4, the free radical trap tests were carried out. Silver nitrate (AN), isopropanol (IPA), disodium edetate (EDTA-2Na) and benzoquinone (BQ) were added to the reaction solution as electrons, $^{\bullet}OH$, hole, and $^{\bullet}O_2^-$ radical scavenger, respectively.[4] As shown in Fig. 6a, the photocatalytic performance of WO_3 for the degradation of RhB is very poor. IPA and EDTA-2Na have almost no effect on the photocatalytic degradation process. However, AN and BQ obviously accelerate the photocatalytic rate of WO_3 for RhB. The mechanism may be that after the consumption of the photogenerated electrons by AN, the photogenerated electron/hole recombination rate becomes lowered, the photogenerated hole concentration increased, and the oxidation rate of RhB over WO_3 is increased. And the comsumption of $^{\bullet}O_2^-$ also accelerate the photocatalytic activity, which may be due to that the adsorption of $^{\bullet}O_2^-$ on the surface can become new trap for h^+.

Therefore, h^+ is the main active species. As shown in Fig. 6b, the effect of IPA and BQ is negligible. EDTA-2Na significantly reduces the photocatalytic activity of WA-60, AN also has a weakly influence, which indicates that the increase of photogenerated hole concentration by the electrons consumption is

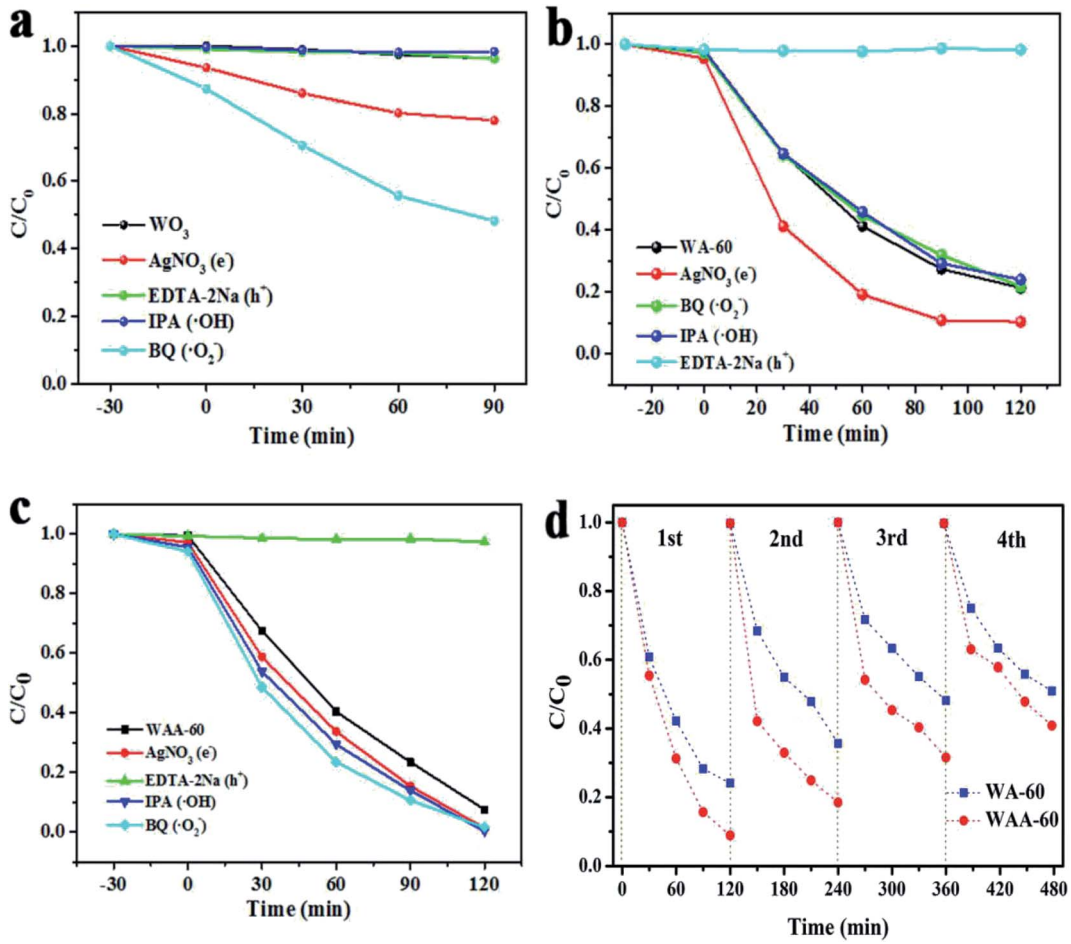

Fig. 6 The degradation of RhB over WO_3 (a), WA-60 (b), and WAA-60 (c) in the presence of different scavengers, and stability tests of WA-60 and WAA-60 (d).

responsible for the increase in photocatalytic activity. Hence, h^+ is still the active species. For WAA-60, EDTA-2Na significantly inhibits the photocatalytic activity, and the other scavengers basically have no effect, indicating that h^+ is the main active substance.

It is well known that the Ag_3PO_4 catalyst can be photocorroded during the photoreaction, so the stability is an important factor for Ag_3PO_4-related catalyst. Recycling performances of RhB degradation over WAA-60 and AW-60 were performed to evaluate their photocatalytic stability. As shown in Fig. 6d, the degradation rate of RhB over WA-60 decreased from 77% to 48% after four recycling runs. In contrast, the photodegradation of RhB over WAA-60 is 92% in the first cycle, and about 59% of the photodegradation ability is retained after five cycles, indicating a stability almost equal to WA-60 under visible light irradiation. Hence, anchoring some Ag nanoparticles between Ag_3PO_4 and WO_3 does not effectively prevent the photocorrosion of Ag_3PO_4.

3.3 Discussion on the mechanism

As shown in Fig. 7a, the optical properties of pure Ag_3PO_4, WO_3, WA-x and WAA-x composites were investigated by ultraviolet-visible diffuse reflectance spectroscopy (DRS). The absorption edge wavelengths of silver phosphate and WO_3 are 525 nm and 461 nm, respectively, showing that both Ag_3PO_4 and WO_3 can absorb visible light. The absorption edges of all composite catalysts after recombination are located between WO_3 and silver phosphate, indicating that the construction of heterojunction can change the light absorption of the catalyst. The band gap energy of pure Ag_3PO_4 and WO_3 can be estimated by the following formula:[49]

$$\alpha h\nu = A(h\nu - E_g)^{n/2} \quad (1)$$

where α, h, ν, E_g, and A refer to absorption coefficient, Planck constant, optical frequency, band gap energy, and constant, respectively. The value of the index n depends on the transition characteristics of the semiconductor with the value of 2 for direct band conversion or 1/2 for indirect band conversion. The fitting results are shown in Fig. 7b, the band gap (E_g) of Ag_3PO_4 being *ca.* 2.36 eV and that of WO_3 being *ca.* 2.67 eV according to eqn (1).[22] The optical absorption edges of pure Ag_3PO_4 and WO_3 are approximately 525 nm and 461 nm, respectively. Compared with pure WO_3, WA-x composites exhibit stronger visible light absorption ability due to the high visible light adsorption of

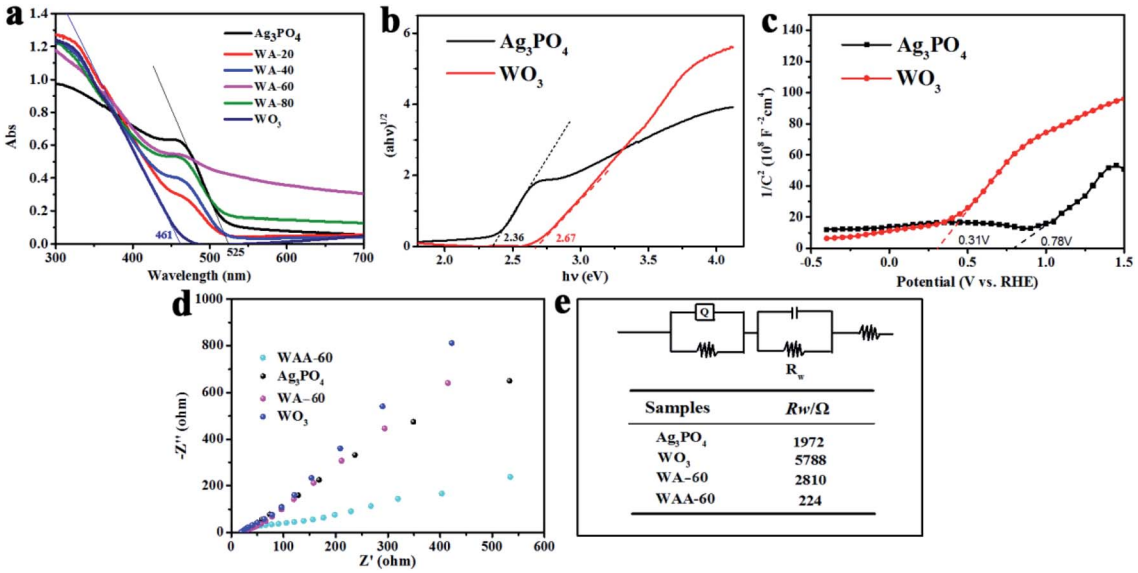

Fig. 7 UV-Vis spectra of Ag_3PO_4, WO_3, and WA-*x* (a); band gap energies of WO_3 and Ag_3PO_4 (b); MS of the Ag_3PO_4, and WO_3 (c); EIS of Ag_3PO_4, WO_3, WAA-0, and WAA-60 (d); and the corresponding fitting results (e).

Ag_3PO_4 nanoparticles deposited on the surface of WO_3 sheets.[50] It is worth noting that the absorption strength of WO_3/Ag_3PO_4 composites is obviously enhanced in the whole region, indicating that WO_3/Ag_3PO_4 composites can enhance the light absorption under visible light attributing to the narrow band gap of Ag_3PO_4 and the synergistic effect between WO_3 and Ag_3PO_4.[51] In addition, as shown in Fig. 7a, the shoulder peak at 480 nm of Ag_3PO_4 can be attributed to the Ag^+/Ag redox peak.

The EIS plots of Ag_3PO_4, WO_3, WA-60, and WAA-60 over the frequency range of 10 mHz to 100 kHz with an amplitude of 5 mV are shown in Fig. 7d. The results show that the R_w of WAA-60 is much smaller than that of WA-60,[52] which indicates that the formation of Ag nanoparticles significantly enhances the transfer activities of photogenerated carriers. Next, the flow of interface electrons between WO_3 and Ag_3PO_4 will be explained.

The results of the band diagrams of WO_3 and Ag_3PO_4 are shown in Fig. 8a, where the work function (Φ) of WO_3, Ag_3PO_4, and WAA-60 are 4.99, 5.47, and 5.44 eV, respectively. According to the information of the work function mapping, the formation of the opposite interfacial electric field of the $WO_3/Ag/Ag_3PO_4$ ternary composite structure can be explained and shown in Fig. 8b. Since Ag is a good conductor, the free electron can transfer from WO_3 to Ag, and then from Ag to Ag_3PO_4 until the Fermi levels of the three components are aligned under thermal equilibrium. Therefore, the space-charge region formed at either side of metal Ag is completely inverse in electric field orientation (accumulation layer at Ag/WO_3 interface and depletion layer at the Ag/Ag_3PO_4 interface, respectively). When the $WO_3/Ag/Ag_3PO_4$ composite is under irradiation, holes in Ag_3PO_4 will transfer to WO_3 and electron in WO_3 will transfer to Ag_3PO_4 under the influence of the interfacial electric field.[52] The driving force of electron transfer is assigned to the difference in Fermi levels between WO_3 and Ag_3PO_4. When the surface state is not considered, its energy band structure is shown in Fig. 8a. When the surface state is considered, the surface band of WO_3 is bent to form a hole accumulation layer, and an electron accumulation layer is formed on the surface of Ag_3PO_4. Therefore, after coupling with Ag_3PO_4, the oxidation capacity of WO_3 is remarkably enhanced due to both the rise in the valence band potential and the decrease in the recombination rate. The introduction of Ag as a medium further reduces the electron transport resistance and further reduces the influence of the interface.

To analyze the flow direction of photogenerated electrons/holes at the WO_3/Ag_3PO_4 interface, the Tafel curves of WO_3 and Ag_3PO_4 were tested under visible light irradiation. As shown in Fig. 8c, the open circuit voltage of WA-60 is 0.41 V (*vs.* NHE) (the blue dashed line in Fig. 8c). According to the Tafel curves of WO_3 and Ag_3PO_4, electrons will flow from WO_3 to Ag_3PO_4. In addition, the ζ potential of WO_3, Ag_3PO_4, WA-60, and WAA-60 were measured in aqueous solution and RhB solution, respectively, as shown in Fig. 8d. The observed values of ζ of as-prepared samples range from -44.5 to -63.6 mV, indicating that their suspensions are stable because of the electrostatic repulsion between the same charged species. The negative charges on the surface of the sample particles are due to the loss of photogenerated holes by oxidation reaction, again confirming the conclusion of the free radical trapping experiments. The ζ potential of WO_3 rises rapidly in the RhB solution, indicating the characteristic adsorption of the RhB cation over WO_3 within the outer Helmholtz plane (OHP). The composite catalysts have more negative ζ potential indicating that the oxidation activity is further increased after the coupling between WO_3 and Ag_3PO_4, but Ag_3PO_4 component reduces the characteristic adsorption of the RhB cation. When RhB^+ is selectively adsorbed on the surface of the catalyst, the appearance of the surface state greatly affects the energy band structure of the catalyst and causes the band to bend upward, which further improves the

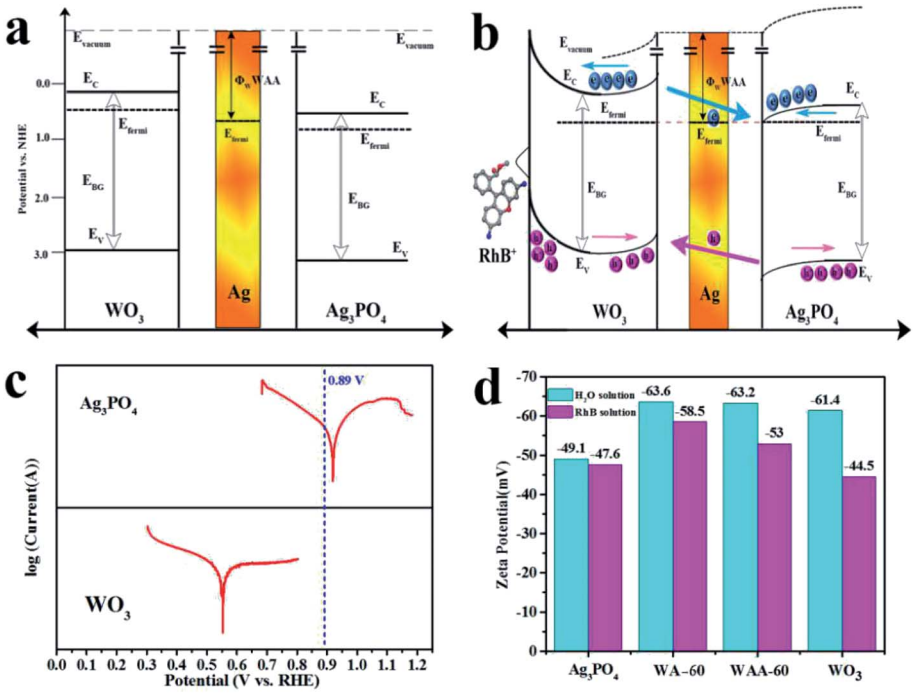

Fig. 8 The band structure of Ag_3PO_4 and WO_3 (a); the electron flow between Ag_3PO_4 and WO_3 (b); Tafel curves of Ag_3PO_4 and WO_3 under irradiation (c); the zeta potential of Ag_3PO_4, WO_3, and WAA-60 measured in aqueous solution and 20 mg L^{-1} RhB solution (d).

oxidizing ability of the hole of WO_3 and limits the reducing ability of Ag_3PO_4. Therefore, the photocatalytic properties of the WA-*x* and WAA-*x* series are significantly affected by the band structure and adsorption of the composite catalyst.

4. Conclusion

The WO_3/Ag_3PO_4 composite photocatalysts were prepared by ultrasonic assisted two-step deposition method. Amongst, WA-60 shows the strongest photocatalytic activity for RhB, which indicates that the weight ratio of WO_3/Ag_3PO_4 plays an important role in the catalytic process. And the photocatalytic activity of the WAA-60 towards the photodegradation of RhB is enhanced near 2 times compared to WA-60, suggesting that the introduction of Ag at the interface increases the degradation activity, which was confirmed by XRD, XPS, SEM, TEM, Raman, and FTIR. Moreover, the trapping experiment results indicate that the holes are the active species in the photodegradation process of RhB over WO3, WA-*x*, and WAA-*x*, the electrons flow from WO_3 to Ag_3PO_4 have be confirmed by DRS, MS, EIS, work function, and zeta potential tests. The introduction of Ag nanoparticles at the interface greatly enhances the mobility of photogenerated carriers.

Availability of data and materials

The authors declare that materials and date are promptly available to readers without undue qualifications in material transfer agreements. All date generated in this study are included in this article.

Authors' contributions

Rui Guo and Shengqi Zhang carried out the laboratory experiment and drafted the manuscript. The other authors provided assistance with the experimental measurements and data analysis. All authors read and approved the final manuscript.

Conflicts of interest

The authors declare that they have no competing interests.

Acknowledgements

This work was supported by the National Natural Science Foundation of China (Grant No. 51704064, 51971058), the Fundamental Research Funds for the Central Universities (Grant N182312007, N2023001), the Program for Liaoning Innovative Talents in University (No. LCR2018016), the Liaoning Provincial Natural Science Foundation of China (No. 2019-MS-244) and the LiaoNing Revitalization Talents Program (No. XLYC1907031).

References

1 M. N. Chong, B. Jin, C. W. K. Chow and C. Saint, Recent developments in photocatalytic water treatment technology: a review, *Water Res.*, 2010, **44**, 2997–3027, DOI: 10.1016/j.watres.2010.02.039.

2 Y. L. Liao, P. Deng, X. Y. Wang, D. N. Zhang, F. M. Li, Q. H. Yang, H. W. Zhang and Z. Y. Zhong, A Facile Method

for Preparation of Cu_2O-TiO_2 NTA Heterojunction with Visible-Photocatalytic Activity, *Nanoscale Res. Lett.*, 2018, **13**, 221, DOI: 10.1186/s11671-018-2637-8.

3 R. Guo, A. G. Yan and J. J. Xu, Effects of morphology on the visible-light-driven photocatalytic and bactericidal properties of $BiVO_4$/CdS heterojunctions: A discussion on photocatalysis mechanism, *J. Alloy. Compd.*, 2020, **817**, 153246, DOI: 10.1016/j.jallcom.2019.153246.

4 X. W. Liu, J. J. Xu, Z. Y. Ni, R. C. Wang, J. H. You and R. Guo, Adsorption and visible-light-driven photocatalytic properties of Ag_3PO_4/WO_3 composites: A discussion of the mechanism, *Chem. Eng. J.*, 2019, **356**, 22–33, DOI: .

5 S. M. Adyani and M. Ghorbani, A comparative study of physicochemical and photocatalytic properties of visible light responsive Fe, Gd and P single and tri-doped TiO_2 nanomaterials, *J. Rare Earth.*, 2018, **36**, 72–85, DOI: 10.1016/j.jre.2017.06.012.

6 J. Di, H. Yang, T. Xian and X. J. Chen, Facile Synthesis and Enhanced Visible-Light Photocatalytic Activity of Novel p-Ag_3PO_4/n-$BiFeO_3$ Heterojunction Composites for Dye Degradation, *Nanoscale Res. Lett.*, 2018, **13**, 257, DOI: 10.1186/s11671-018-2671-6.

7 X. Zheng, H. Yang, Z. M. Cui, H. M. Zhang and X. X. Wang, A novel $Bi_4Ti_3O_{12}$/Ag_3PO_4 heterojunction photocatalyst with enhanced photocatalytic performance, *Nanoscale Res. Lett.*, 2017, **12**, 608, DOI: 10.1186/s11671-017-2377-1.

8 J. H. You, Y. Z. Guo, R. Guo and X. W. Liu, A review of visible light-active photocatalysts for water disinfection: Features and prospects, *Chem. Eng. J.*, 2019, **373**, 624–641.

9 X. W. Liu, Z. Y. Ni and Y. He, Ultrasound-assisted two-step water-bath synthesis of g-C_3N_4/BiOBr composites: visible light-driven photocatalysis, sterilization, and reaction mechanism, *New J. Chem.*, 2019, **43**, 8711–8721.

10 Q. W. Cao, Y. F. Zheng and X. C. Song, Enhanced visible-light-driven photocatalytic degradation of RhB by $AgIO_3$/WO_3 composites, *J. Taiwan Inst. Chem. Eng.*, 2017, **70**, 359–365, DOI: 10.1016/j.jtice.2016.10.030.

11 T. T. Xiao, Z. Tang, Y. Yang, L. Q. Tang, Y. Zhou and Z. G. Zou, In situ construction of hierarchical WO_3/g-C_3N_4 composite hollow microspheres as a Z-Scheme photocatalyst for the degradation of antibiotics, *Appl. Catal., B*, 2018, **220**, 417–428, DOI: 10.1016/j.apcatb.2017.08.070.

12 W. L. Yu, J. X. Chen, T. T. Shang, L. F. Chen, L. Gu and T. Y. Peng, Direct Z-scheme g-C_3N_4/WO_3 photocatalyst with atomically defined junction for H_2 production, *Appl. Catal., B*, 2017, **219**, 693–704, DOI: 10.1016/j.apcatb.2017.08.018.

13 P. Wang, N. Lu, Y. Su, N. Liu, H. T. Yu, J. Li and Y. Wu, Fabrication of WO_3@g-C_3N_4 with core@shell nanostructure for Enhanced photocatalytic degradation activity under visible light, *Appl. Surf. Sci.*, 2017, **423**, 197–204, DOI: 10.1016/j.apsusc.2017.06.127.

14 J. Zhang, Y. Guo, Y. H. Xiong, D. D. Zhou and S. S. Dong, An environmentally friendly Z-scheme WO_3/CDots/CdS heterostructure with remarkable photocatalytic activity and anti-photocorrosion performance, *J. Catal.*, 2017, **356**, 1–13, DOI: 10.1016/j.jcat.2017.09.021.

15 B. Song, T. T. Wang, H. G. Sun, Q. Shao, J. K. Zhao, K. K. Song, L. H. Hao, L. Wang and Z. H. Guo, Two-step hydrothermally synthesized carbon nanodots/WO_3 photocatalysts with enhanced photocatalytic performance, *Dalton Trans.*, 2017, **45**, 15769–15777, DOI: 10.1039/C7DT03003G.

16 H. B. Fan, Q. F. Ren, S. L. Wang, Z. Jin and Y. Ding, Synthesis of the Ag/Ag_3PO_4/diatomite composites and their enhanced photocatalytic activity driven by visible light, *J. Alloys Compd.*, 2019, **775**, 845–852, DOI: 10.1016/j.jallcom.2018.10.152.

17 J. S. Lu, Y. J. Wang, F. Liu, L. Zhang and S. N. Chai, Fabrication of a direct Z-scheme type WO_3/Ag_3PO_4 composite photocatalyst with enhanced visible-light photocatalytic performances, *Appl. Surf. Sci.*, 2017, **393**, 180–190, DOI: 10.1016/j.apsusc.2016.10.003.

18 H. Xu, H. Z. Zhao, Y. G. Xu, Z. G. Chen, L. Y. Huang, Y. P. Li, Y. H. Song, Q. Zhang and H. M. Li, Three-dimensionally ordered macroporous WO_3 modified Ag_3PO_4 with enhanced visible light photocatalytic performance, *Ceram. Int.*, 2016, **42**, 1392–1398, DOI: 10.1016/j.ceramint.2015.09.081.

19 Y. Chang, K. Yu, C. X. Zhang, R. Li, P. Y. Zhao, L. L. Lou and S. X. Liu, Three-dimensionally ordered macroporous WO_3 supported Ag_3PO_4 with enhanced photocatalytic activity and durability, *Appl. Catal., B*, 2015, **176**, 363–373, DOI: 10.1016/j.apcatb.2015.04.017.

20 Y. Y. Bu, Z. Y. Chen and C. J. Su, Highly efficient Z-Scheme Ag_3PO_4/Ag/WO_{3-x} photocatalyst for its enhanced photocatalytic performance, *Appl. Catal., B*, 2015, **179**, 363–371, DOI: 10.1016/j.apcatb.2015.05.045.

21 L. Cai, X. L. Xiong, N. G. Liang and Q. Y. Long, Highly effective and stable Ag_3PO_4-WO_3/MWCNTs photocatalysts for simultaneous Cr (VI) reduction and orange II degradation under visible light irradiation, *Appl. Surf. Sci.*, 2015, **353**, 939–948, DOI: 10.1016/j.apsusc.2015.07.028.

22 Q. Y. Li, F. L. Wang, Y. X. Hua, Y. T. Luo, X. H. Liu, G. R. Duan and X. J. Yang, Deposition-precipitation Preparation of Ag/Ag_3PO_4/WO_3 Nanocomposites for efficient Visible-light Degradation of Rhodamine B under Strongly Acidic/Alkaline conditions, *J. Colloid Interf. Sci.*, 2017, **506**, 207–216, DOI: 10.1016/j.jcis.2017.07.018.

23 C. Wang, M. M. Wu, M. Yan, H. Q. Shen, F. P. Cai, B. Hu and W. D. Shi, Enhanced visible-light photocatalytic activity and the mechanism study of WO_3 nanosheets coupled with Ag_3PO_4 nanocrystals, *Ceram. Inter.*, 2015, **41**, 6784–6792, DOI: 10.1016/j.ceramint.2015.01.125.

24 J. Q. Zhang, K. Yu, Y. F. Yu, L. L. Lou, Z. Q. Yang, J. W. Yang and S. X. Liu, Highly effective and stable Ag_3PO_4/WO_3 photocatalysts for visible light degradation of organic dyes, *J. Mol. Catal. A: Chem.*, 2014, **391**, 12–18, DOI: 10.1016/j.molcata.2014.04.010.

25 S. Y. Zhang, H. Li and Z. F. Yang, Controllable synthesis of WO_3 with different crystalline phases and its applications on methylene blue removal from aqueous solution, *J. Alloys Compd.*, 2017, **722**, 555–563, DOI: 10.1016/j.jallcom.2017.06.095.

26 J. Ding, Q. Q. Liu, Z. Y. Zhang, X. Liu, J. Q. Zhao, S. B. Cheng, B. N. Zong and W. L. Dai, Carbon nitride nanosheets decorated with WO_3 nanorods: ultrasonic-assisted facile synthesis and catalytic application in the green manufacture of dialdehydes, *Appl. Catal., B*, 2015, **165**, 511–518, DOI: 10.1016/j.apcatb.2014.10.037.

27 J. Ma, J. Zou, L. Li, C. Yao, T. Zhang and D. Li, Synthesis and characterization of Ag_3PO_4 immobilized in bentonite for the sunlight-driven degradation of Orange II, *Appl. Catal., B*, 2013, **134–135**, 1–6, DOI: 10.1016/j.apcatb.2012.12.032.

28 L. F. Lopes, F. M. Pontes, L. O. Garcia, D. S. L. Pontes, D. Padovani, A. J. Chiquito, S. R. Teixeira, Y. N. Colmenares, V. R. Mastelaro and E. Longo, Silver-controlled evolution of morphological, structural, and optical properties of three-dimensional hierarchical WO_3 structures synthesized from hydrothermal method, *J. Alloys Compd.*, 2018, **736**, 143–151, DOI: 10.1016/j.jallcom.2017.11.095.

29 B. Chai, J. Li and Q. Xu, Reduced graphene oxide grafted Ag_3PO_4 Composites with efficient photocatalytic activity under visible-light irradiation, *Ind. Eng. Chem. Res.*, 2014, **53**, 8744–8752, DOI: 10.1021/ie4041065.

30 M. Y. Zhou, H. X. Shi, H. W. Huang, F. Chen, Y. T. Li, K. Wang and Y. H. Zhang, $Bi_2O_2(OH)NO_3$/AgI heterojunction with enhanced UV and visible-light responsive photocatalytic activity and mechanism investigation, *Mater. Res. Bull.*, 2018, **108**, 120–129, DOI: 10.1016/j.materresbull.2018.08.039.

31 E. Grilla, A. Petala, Z. Frontistis, I. K. Konstantinou, D. I. Kondarides and D. Mantzavinos, Solar photocatalytic abatement of sulfamethoxazole over Ag_3PO_4/WO_3 composites, *Appl. Catal., B*, 2018, **231**, 73–81, DOI: 10.1016/j.apcatb.2018.03.011.

32 B. Ayoubi-Feiz, M. H. Mashhadizadeh and M. Sheydaei, Degradation of diazinon by new hybrid nanocomposites N-TiO_2/Graphene/Au and N-TiO_2/Graphene/Ag using visible light photo-electro catalysis and photo-electro catalytic ozonation: Optimization and comparative study by Taguchi method, *Sep. Purif. Technol.*, 2019, **211**, 704–714, DOI: 10.1016/j.seppur.2018.10.032.

33 C. X. Zheng and H. Yang, Assembly of Ag_3PO_4 nanoparticles on rose flower-like Bi_2WO_6 hierarchical architectures for achieving high photocatalytic performance, *J. Mater. Sci.: Mater. Electron.*, 2018, **29**, 9291–9300, DOI: 10.1007/s10854-018-8959-6.

34 N. K. Eswar, V. V. Katkar, P. C. Ramamurthy and G. Madras, Novel AgBr/Ag_3PO_4 decorated ceria nanoflake composites for enhanced photocatalytic activity toward dyes and bacteria under visible light, *Ind. Eng. Chem. Res.*, 2015, **54**, 8031–8042, DOI: 10.1021/acs.iecr.5b01993.

35 B. J. Jiang, Y. H. Wang, J. Q. Wang, C. G. Tian, W. J. Li, Q. M. Feng, Q. J. Pan and H. G. Fu, In situ fabrication of Ag/Ag_3PO_4/graphene triple heterostructure visible-light photocatalyst through graphene-assisted reduction strategy, *ChemCatChem*, 2013, **5**, 1359–1367, DOI: 10.1002/cctc.201200684.

36 S. Y. Wang, H. Yang, X. X. Wang and W. J. Feng, Surface Disorder Engineering of Flake-Like Bi_2WO_6 Crystals for Enhanced Photocatalytic Activity, *J. Electron. Mater.*, 2019, **48**, 2067–2076, DOI: 10.1007/s11664-019-07045-5.

37 M. L. Yin, L. M. Yu and S. Z. Liu, Synthesis of Ag quantum dots sensitized WO_3 nanosheets and their enhanced acetone sensing properties, *Mater. Lett.*, 2017, **186**, 66–69, DOI: 10.1016/j.matlet.2016.09.083.

38 A. Yan, C. Xie, F. Huang, S. Zhang and S. Zhang, An efficient method to modulate the structure, morphology and properties of WO_3 through niobium doping, *J. Alloys Compd.*, 2014, **610**, 132–137, DOI: 10.1016/j.jallcom.2014.04.188.

39 L. Santos, J. P. Neto, A. Crespo, D. Nunes, N. Costa, I. M. Fonseca, *et al.*, WO_3 Nanoparticle-Based Conformable pH Sensor, *Appl. Mater. Interf.*, 2014, **6**, 12226–12234, DOI: 10.1021/am501724h.

40 Y. Tingfeng, W. Tingting, L. Ying, *et al.*, Efforts on enhancing the Li-ion diffusion coeffificient and electronic conductivity of titanate-based anode materials for advanced Li-ion batteries, *Energy Storage Materials*, 2020, **26**, 165–197, DOI: 10.1016/j.ensm.2019.12.042.

41 A. A. Isari, M. Mehregan, S. Mehregan, F. Hayati, R. R. Kalantary and B. Kakavandi, Sono-photocatalytic degradation of tetracycline and pharmaceutical wastewater using WO_3/CNT heterojunction nanocomposite under US and visible light irradiations: A novel hybrid system, *J. Hazard. Mater.*, 2020, **390**, 122050.

42 S. L. Bai, K. W. Zhang, J. H. Sun, D. F. Zhang, R. X. Luo, D. Q. Li and C. C. Liu, Polythiophene-WO_3 hybrid architectures for low-temperature H_2S detection, *Sens. Actuators, B*, 2014, **197**, 142–148, DOI: 10.1016/j.snb.2014.02.038.

43 C. M. White, J. S. Jang, S. H. Lee, J. Pankow and A. C. Dillon, Photocatalytic Activity and Photoelectrochemical property of Nano-WO_3 Powders Made by Hot-Wire Chemical Vapor Deposition, *Electrochem. Solid-State Lett.*, 2010, **13**, B120–B122, DOI: 10.1149/1.3484474.

44 L. J. Xu, M. L. Yin and S. Z. Liu, Agx@WO_3 core-shell nanostructure for LSP enhanced chemical sensors, *Sci. Rep.*, 2014, **4**, 6745, DOI: 10.1038/srep06745.

45 C. Y. Su, H. C. Lin and C. K. Lin, Fabrication and optical properties of Ti-doped $W_{18}O_{49}$ nanorods using a modified plasma-arc gas-condensation technique, *J. Vac. Sci. Technol., B: Microelectron. Nanometer Struct.–Process., Meas., Phenom.*, 2009, **27**, 2170–2174, DOI: 10.1116/1.3208007.

46 Y. Q. Kong, H. G. Sun, X. Zhao, B. Y. Gao and W. L. Fan, Fabrication of hexagonal/cubic tungsten oxide homojunction with improved photocatalytic activity, *Appl. Catal., A*, 2015, **505**, 447–455, DOI: 10.1016/j.apcata.2015.05.015.

47 X. Q. Wu, J. Zhao, L. P. Wang, M. M. Han, M. L. Zhang, H. B. Wang, H. Huang, Y. Liu and Z. H. Kang, Carbon dots as solid-state electron mediator for $BiVO_4$/CDs/CdS Z-scheme photocatalyst working under visible light, *Appl. Catal., B*, 2017, **206**, 501–509, DOI: 10.1016/j.apcatb.2017.01.049.

48 X. W. Liu, J. H. You, R. C. Wang, Z. Y. Ni, F. Han, L. Jin, Z. Q. Ye, Z. Fang and R. Guo, Synthesis and absorption properties of hollow-spherical $Dy_2Cu_2O_5$ via a coordination compound method with $[DyCu(3,4\text{-}pdc)_2(OAc)(H_2O)_2]\cdot 10.5H_2O$ precursor, *Sci. Rep.*, 2017, **7**, 13085, DOI: 10.1038/s41598-017-13544-4.

49 R. Guo, R. C. Wang, Z. Y. Ni and X. W. Liu, Synthesis and electrochemical performance of Co_3O_4 via a coordination method, *Appl. Phys. A*, 2018, **124**, 623, DOI: 10.1007/s00339-018-1873-1.

50 J. Wan, X. Du, E. Liu, Y. Hu, J. Fan and X. Hu, Z-scheme visible-light-driven Ag_3PO_4 nanoparticle@MoS_2 quantum dot/few-layered MoS_2 nanosheet heterostructures with high efficiency and stability for photocatalytic selective oxidation, *J. Catalys.*, 2017, **345**, 281–294, DOI: 10.1016/j.jcat.2016.11.013.

51 Y. R. Lv, R. Huo, S. Y. Yang, Y. Q. Liu, X. J. Li and Y. H. Xu, Self-assembled synthesis of PbS quantum dots supported on polydopamine encapsulated $BiVO_4$ for enhanced visible-light-driven photocatalysis, *Sep. Purif. Technol.*, 2018, **197**, 281–288, DOI: 10.1016/j.seppur.2018.01.006.

52 Y. Tingfeng, Q. Liying, M. Jie, *et al.*, Porous spherical NiO@NiMoO4@PPy nanoarchitectures as advanced electrochemical pseudocapacitor materials, *Science Bulletin*, 2020, **65**, 546–556, DOI: 10.1016/j.scib.2020.01.011.